Optimized bunch lengthening for beam extraction from J-PARC RCS

Kyosuke Adachi,* Fumihiko Tamura, Masahiro Nomura, Taihei Shimada, Ryosuke Miyakoshi, Hidefumi Okita, Masahito Yoshii, Chihiro Ohmori, Kiyomi Seiya, Keigo Hara, Katsushi Hasegawa, and Yasuyuki Sugiyama

J-PARC Center, Tokai, Ibaraki 319-1195, Japan

(Received 15 April 2026; accepted 21 October 2026; published 10 November 2026)

The 3-GeV rapid-cycling synchrotron (RCS) at Japan Proton Accelerator Research Complex (J-PARC) supplies a high-intensity beam to the Main Ring (MR) synchrotron. Under the present operating conditions, the RCS extraction bunch is intentionally injected into the MR rf bucket in a mismatched condition. This mismatch causes the bunch to dilute within the MR bucket, which rapidly increases the bunching factor B_f, defined as the ratio of average to peak current, and raises it to the desired value immediately after injection. Increasing the bunching factor B_f is essential for reducing beam losses caused by space-charge effects. Although this scheme has been effective for improving B_f, the dilution process also produces oscillations in the bunch profile and leads to local reductions of B_f, which contribute to beam losses immediately after MR injection. To achieve higher beam power in future MR operation, it is therefore desirable to increase B_f before injection into MR, so that beam losses at the beginning of acceleration can be suppressed. A method called "bunch lengthening" has been proposed to stretch the RCS extraction beam bunch. This method stretches the bunch and increases the B_f. It is based on driving a second-harmonic rf voltage in the latter part of acceleration and placing the beam at the unstable fixed point. Experiments on bunch lengthening with low-intensity beams, conducted in RCS and MR, demonstrated the stretching of the RCS extraction beam. The B_f increased from approximately 0.2 to 0.4 in both simulations and beam experiments. These results indicate that the longitudinal beam matching between RCS and MR has improved. To further optimize bunch lengthening, the deformation process of the stretched bunch was investigated. The second-harmonic rf voltage was applied twice with optimized timing, resulting in improved longitudinal matching. A detailed presentation of the bunch lengthening and the results of demonstration tests conducted on the J-PARC synchrotrons is provided. The examination results on the optimization of bunch lengthening are also reported.

DOI: 10.1103/vk96-lb5v

I. INTRODUCTION

The Japan Proton Accelerator Research Complex (J-PARC) consists of the 400-MeV LINAC, the 3-GeV rapid-cycling synchrotron (RCS) [1,2], and the main ring (MR) synchrotron [3]. RCS accepts an H^- beam from the LINAC, converts it to protons by charge-exchange injection, and accelerates it from 400 MeV to 3 GeV. RCS has achieved stable acceleration of high-intensity beams up to the design intensity of 8×10^{13} protons per pulse (ppp), with minimal beam loss. MR accelerates the proton beam delivered by RCS from 3 to 30 GeV. MR is one of the world's most powerful accelerators with a beam intensity of 2×10^{14} ppp. MR achieved 900 kW user operation in 2025. An upgrade is underway to achieve beam power up to 1.3 MW [4].

Space-charge effects are one of the significant causes of beam loss during the acceleration of high-intensity proton beams, such as in MR. The space-charge effect, arising from Coulomb forces between charged particles, significantly affects both longitudinal and transverse beam dynamics, especially at high beam intensity. In the longitudinal beam motion, the space-charge effect occurs as a divergent force and contributes to the reduction of the rf acceleration voltage under transition energy [5]. The space-charge-induced incoherent betatron tune shifts and resonance excitation contribute to transverse emittance growth and beam loss [6]. The tune shift $\Delta\nu_t$ is given by Eq. (1).

$$\Delta\nu_t = -\frac{N_p r_p}{2\pi\epsilon\beta^2\gamma^3 B_f}. \tag{1}$$

*Contact author: kyosuke.adachi@j-parc.jp

Published by the American Physical Society under the terms of the Creative Commons Attribution 4.0 International license. Further distribution of this work must maintain attribution to the author(s) and the published article's title, journal citation, and DOI.

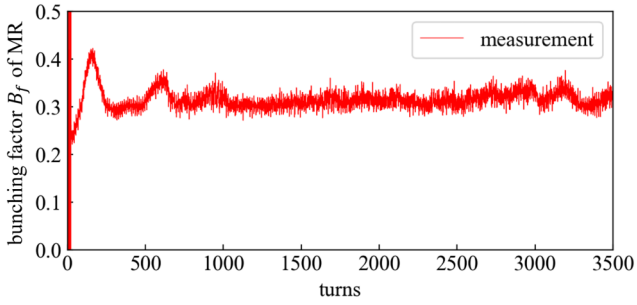


FIG. 1. The measured B_f after injection into MR in 800-kW fast extraction (FX) mode.

Here, N_p denotes the number of particles, r_p is the classical proton radius, and ϵ is the transverse beam emittance. B_f is defined as the ratio of the average current to the peak current, as given in Eq. (2).

$$B_f = \frac{(\text{average current})}{(\text{peak current})}, \tag{2}$$

and it ranges from 0 to 1, where 1 corresponds to a coasting beam. As shown in Eqs. (1) and (2), when B_f is small, the tune shift due to the space-charge forces increases. Increasing B_f of the beam mitigates the space-charge effects.

Under the present operating conditions, RCS delivers short-extraction bunches with a low B_f of approximately 0.2. This low B_f arises because only the fundamental rf voltage is applied during the latter part of RCS acceleration, and adiabatic damping reduces the longitudinal beam width. To accommodate these short bunches, the MR rf bucket employs a dual-harmonic rf operation. The bunch extracted from RCS is injected into the MR rf bucket in a deliberately mismatched condition, causing it to be diluted within the bucket. As the beam is diluted within the bucket, the bunching factor B_f improves rapidly and reaches approximately 0.3 within a short time after injection, as shown in Fig. 1. Although this scheme has been effective for improving B_f, the dilution process also produces oscillations in the bunch profile and leads to local reductions of B_f.

Measured beam losses in MR are on the order of $\sim$1% [7], and most of them occur immediately after injection, where the bunching factor B_f locally decreases, and the space-charge effect becomes strongest. Therefore, suppressing the decrease in B_f immediately after injection and mitigating the resulting space-charge effect are essential for reducing beam loss and achieving higher beam intensity in MR. We investigated a method in which the bunch length of the RCS extraction beam is increased to raise B_f, enabling beam injection into MR in a matched condition with the MR rf bucket, unlike the conventional mismatched injection scheme. This approach prevents the decrease of B_f immediately after injection.

Several methods have been proposed for manipulating the longitudinal phase-space distribution, including adiabatic and nonadiabatic voltage reduction, as well as bunch lengthening along the unstable fixed point (UFP) generated by the fundamental rf voltage. These techniques were previously studied as bunch compression methods at CERN PS and Fermilab [8–10]. These approaches do not assume bunch manipulation during acceleration and therefore are not suitable for high-intensity proton booster rings. In RCS, bunch lengthening must be performed during acceleration, and moreover, it must be carried out rapidly in the latter part of the cycle, where the slip factor becomes very small (approximately −0.05). Under these conditions, the conventional methods are not effective in this situation. Details of RCS operating conditions are described in Sec. II.

Based on these considerations, nonadiabatic methods have been proposed for stretching the bunch length in RCS [11]. This method is based on applying the V_{h4} (second-harmonic rf voltage) in the latter part of acceleration and placing the beam at UFP. The fundamental rf voltage V_{h2} continues to provide acceleration, while the second-harmonic rf voltage is dedicated to bunch lengthening, creating a clear division of roles.

This configuration establishes the UFP inside the stable region and offers high flexibility for controlling the bunch length. Furthermore, in this study, we introduce a least-squares-based optimization procedure to determine the rf voltage pattern, enabling a systematic approach for guiding the shape of the bunch toward a desired target distribution during acceleration. These new bunch lengthening techniques are expected to be useful not only for RCS but also for future high-intensity proton booster rings as a means of mitigating beam loss caused by the space-charge effects.

This paper is organized as follows. Section II describes rf and low-level rf (LLRF) systems for RCS. Section III introduces the concept of bunch lengthening using the UFP. An example of the rf voltage pattern of the V_{h4} is presented, followed by longitudinal beam simulation results. Section IV focuses on optimizing the rf voltage pattern by analyzing the bunch deformation process to realize the bunch shape that improves longitudinal matching with MR. Section V presents demonstration results of bunch lengthening and the bunch-shape optimization.

II. RF SYSTEM OVERVIEW OF THE J-PARC RCS

The main parameters of RCS and its rf system are summarized in Table I. A 400-MeV proton beam injected from the LINAC is accelerated to 3 GeV within 20 ms. RCS operates at a repetition rate of 25 Hz and delivers high-intensity proton beams to the Materials and Life Science Experimental Facility and to MR.

TABLE I. The parameters of the J-PARC RCS.

Circumference	348.333 m
Energy	0.400–3 GeV
Beam intensity	(achieved) 8.33×10^{13} ppp
Accelerating frequency	1.227–1.671 MHz
Fundamental harmonic number	2
Driving harmonics	2 and 4
Repetition rate	25 Hz
Momentum compaction factor	0.012
No. of cavities	12
Q-value of rf cavity	2

Twelve rf cavities are installed in RCS to generate a maximum accelerating voltage of 440 kV for acceleration of high-intensity proton beams. Each cavity is loaded with a magnetic-alloy (MA) core [12], whose broadband frequency response ($Q \simeq 2$) covers not only the fundamental accelerating frequency range from 1.23 to 1.67 MHz (harmonic $h = 2$), corresponding to the beam velocity change, but also the second-harmonic component ($h = 4$). Figure 2 shows a typical accelerating rf voltage pattern used for beam delivery to MR. RCS employs dual-harmonic operation, utilizing the fundamental rf voltage V_{h2} and the second-harmonic rf voltage V_{h4} at the beginning of acceleration to mitigate the space-charge effects at injection.

Because the MA cavities are broadband, the wake voltage induced by the high-intensity proton beam contains not only the fundamental component but also significant higher-harmonic components. To control the rf voltage and compensate for beam loading, a LLRF control system is implemented [13]. The LLRF system incorporates a multiharmonic vector rf voltage control feedback to suppress wake voltages containing multiple harmonic components [14].

This feedback consists of blocks for each harmonic ($h = 1 \cdots 8$), where the detected I/Q cavity voltage is compared with the corresponding I/Q voltage pattern, and the error is processed through PI control and I/Q modulation to generate the feedback output. By employing frequency-indexed phase-offset and gain look-up tables, stable control over the wide harmonic range ($h = 1 \cdots 8$) is achieved using a single PI gain. With this digital control logic based on I/Q signal processing, the LLRF system enables simultaneous control of higher-harmonic components ($h = 1 \cdots 8$) while maintaining fast response required for high-intensity proton acceleration.

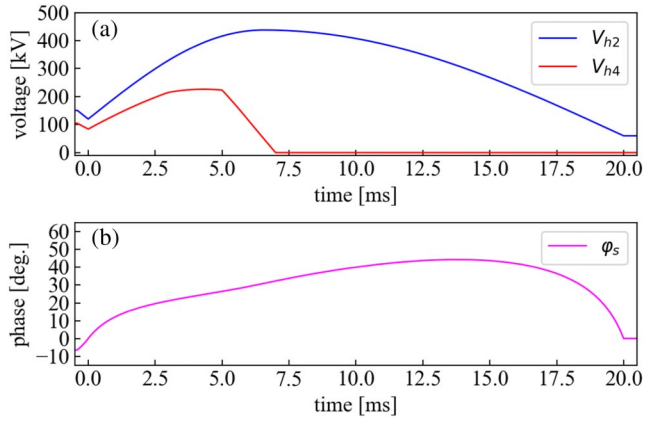


FIG. 2. RF voltage patterns of RCS in the current MR 800-kW FX mode: (a) voltage and (b) synchronous phase ϕ_s.

III. BUNCH LENGTHENING USING SECOND HARMONIC RF VOLTAGE

The schematic view of the bunch lengthening using the UFP generated by V_{h4} is shown in Fig. 3. Assuming a negative slip factor ($\eta < 0$) and a synchronous phase of $\phi_s = 0$, the following configuration is considered. The V_{h2} is shown by a cyan dotted line, and the V_{h4} is shown by a

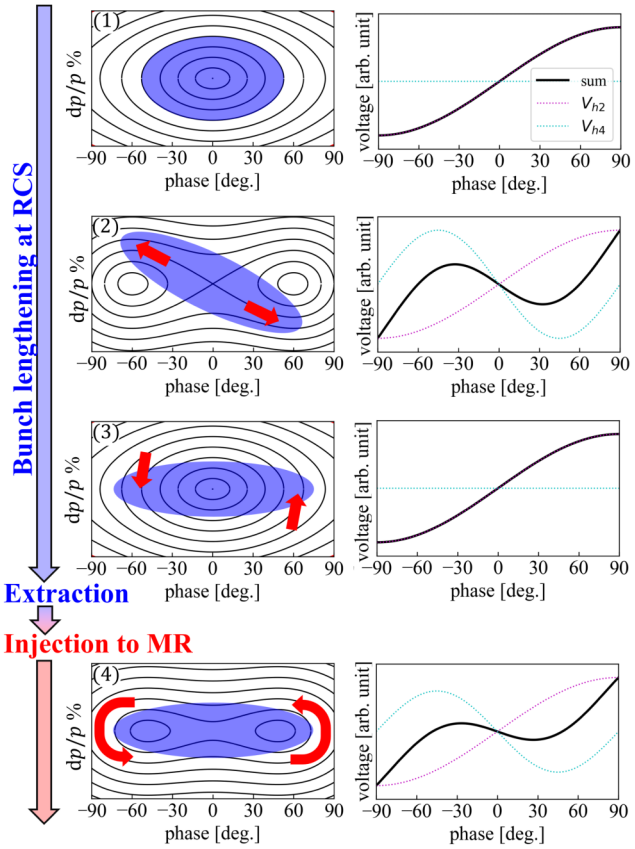


FIG. 3. The illustration shows the scheme of bunch lengthening using the UFP. (Left) Longitudinal phase-space distributions on the Hamiltonian contours, with red arrows indicating the deformation direction. (Right) Fundamental and second-harmonic rf voltages, V_{h2} and V_{h4}, and their superposition. Panels (1)–(3) show the bunch lengthening process in RCS just before extraction: (1) initial state, (2) stretching by V_{h4}, and (3) rotation under V_{h2}. Panel (4) illustrates the stretched bunch injected into MR and the corresponding dual-harmonic bucket.

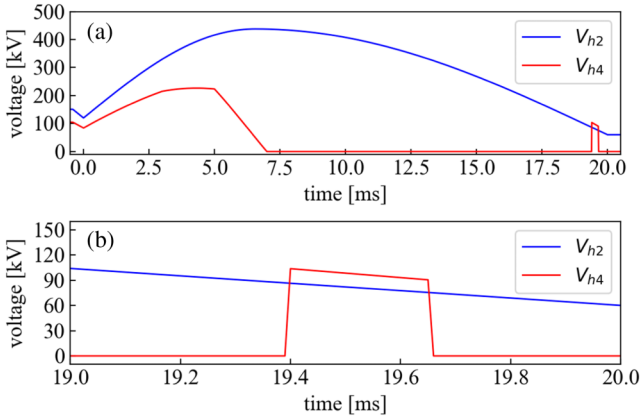


FIG. 4. The upper graph (a) shows the rf voltage pattern, where V_{h4} is applied in the latter part of the acceleration cycle. The lower graph (b) shows an expanded view of the latter part of acceleration (19.0–20.0 ms) in the upper graph.

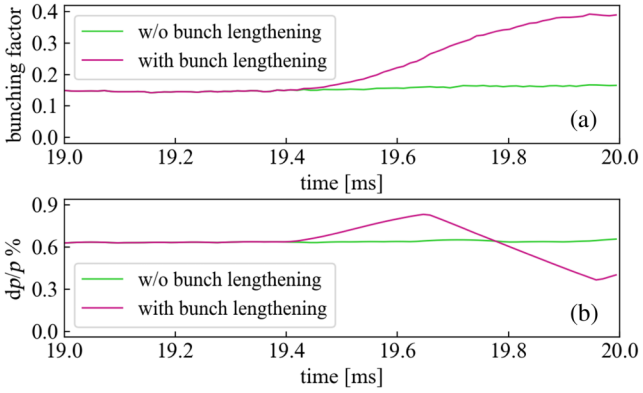


FIG. 5. Comparison with and without the V_{h4} in the latter part of acceleration. Panel (a) shows B_f, and panel (b) shows the maximum dp/p of the bunch at each moment during the bunch lengthening process. The green line represents the case without bunch lengthening, whereas the purple line represents the case with bunch lengthening.

magenta dotted line. The black solid line represents the superposed voltage $(V_{h2} + V_{h4})$. The UFP is generated at the bunch center position. As shown by the red arrows, the bunch is stretched in the direction along the contour line around the UFP. After stretching, the bunch is rotated while preserving its stretched shape by applying only the V_{h2}.

In our operation scheme, the bunch lengthening and the increase of the bunching factor are completed in RCS before extraction, rather than being produced by an intentional mismatch after injection into MR. After extraction, the stretched bunch is injected into MR as a beam already matched to the dual-harmonic bucket.

The potential term $U(\phi)$ of the Hamiltonian with the V_{h4} superposed is given in Eq. (3). The phase of the V_{h4} is determined so as not to affect the acceleration of synchronized particles by the V_{h2}. As shown in Fig. 3, the UFP is generated when the voltage slope becomes negative around ϕ_s. The condition for the generation of a UFP positioned at the ϕ_s is provided by Eq. (4).

$$U(\phi) = \frac{eV_{h2}}{2\pi h}\left[\cos(\phi) + \phi\sin(\phi_s) - \frac{1}{2}\frac{V_{h4}}{V_{h2}}\cos(2(\phi-\phi_s))\right], \tag{3}$$

$$\frac{V_{h4}}{V_{h2}} > \frac{1}{2}\cos(\phi_s), \tag{4}$$

where, h denotes the harmonic number.

TABLE II. Parameters of the UFP Pattern.

Time	19.40–19.65 ms
Ratio (V_{h4}/V_{h2})	1.2
Rise and fall time	0.01 ms

Figure 4 shows an example of the rf voltage pattern of bunch lengthening with the V_{h4}, hereafter referred to as the UFP pattern. The corresponding parameters are listed in Table II. The beam extraction timing was set to 15 450 turns (20 ms), and the application period of the V_{h4} was adjusted so that a stretched bunch was formed at this timing. The rise and fall times of the V_{h4} were set to

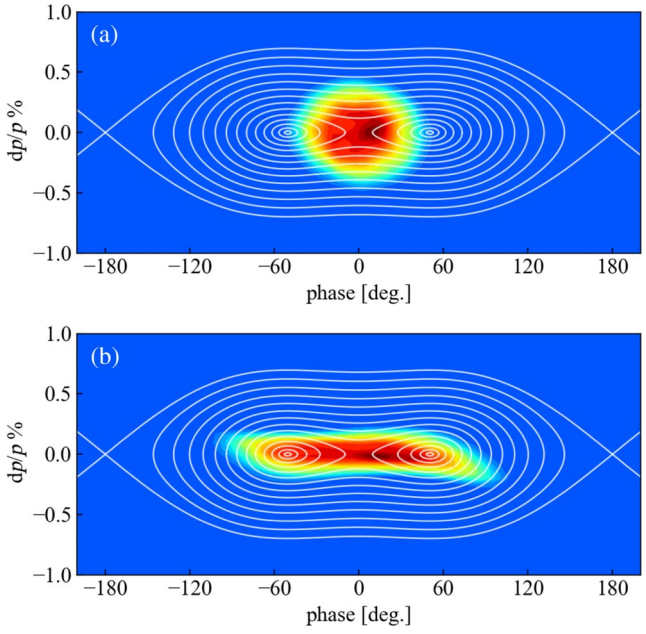


FIG. 6. The phase-space distribution of the stretched RCS extraction beam on the MR rf bucket. The MR rf bucket shape and contour lines are for MR operating in 800-kW FX mode. The upper panel (a) shows the phase-space distribution without bunch lengthening, while the lower panel (b) shows the distribution with bunch lengthening.

0.01 ms. The amplitude of V_{h4} was determined from the voltage ratio V_{h4}/V_{h2}.

Figure 5 shows the B_f and $\mathrm{d}p/p$ in the latter part of acceleration when bunch lengthening is applied. The green line represents the simulation result for the normal operating mode, whereas the purple line represents the case with bunch lengthening. B_f increases to about 0.4 within approximately 0.6 ms immediately before extraction, while $\mathrm{d}p/p$ remains below 1%. Figure 6 compares the phase-space distributions of the RCS extraction beam in the MR rf bucket for cases without and with bunch lengthening. These findings indicate that the application of bunch lengthening increases bunch width. These simulation results were obtained using Beam Longitudinal Dynamics (BLonD), a longitudinal beam simulation code developed at CERN [15].

IV. OPTIMIZATION OF THE UFP PATTERN FOR BUNCH LENGTH AND SHAPE CONTROL

Creating a UFP pattern that delivers beams satisfying downstream requirements on bunch length and shape is essential. To achieve this, it is necessary to understand how variations in each parameter of the UFP pattern affect the resulting bunch width, B_f, and the bunch shape.

A. Control of bunch length

As shown in Fig. 7, the bunch width and B_f depend on the application period and the voltage ratio (V_{h4}/V_{h2}), which are parameters of the UFP pattern. A longer application period of the V_{h4} leads to a higher B_f. When the V_{h4}/V_{h2} is large, the required application period of the V_{h4} can be shortened. Conversely, when V_{h4}/V_{h2} is small, the bunch width is shorter for the same B_f. These results indicate the flexible tunability of the bunch width and B_f using the bunch lengthening. In addition, both B_f and the bunch width exhibit peak values depending on the application period. As illustrated by the potential and contour plots in Fig. 3, if the application period is too long, the symmetric fixed points (SFPs) on both sides bend the tips of the stretched bunch in a direction different from that indicated by the red arrow in panel (2) of the left column in Fig. 3. As a result, the phase-space distribution becomes complex, the bunch width shortens, and B_f decreases.

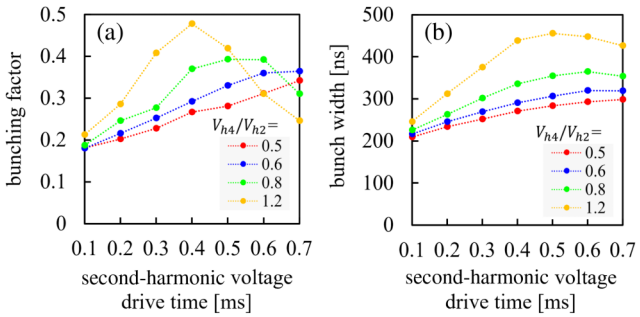


FIG. 7. Changes in the B_f and width of the RCS extraction beam obtained using UFP patterns parameterized by the V_{h4} application period and the voltage ratio. The horizontal axis represents the application period of the V_{h4}, while the vertical axis shows (a) B_f and (b) the bunch width.

Next, control of the bunch shape is considered. As shown in Fig. 6, the stretched bunch has a shape similar to a parallelogram. The sharp corners of the parallelogram, hereafter referred to as the tail, form filamentation structures after MR injection. When a tail is present, the phase-space distribution becomes significantly broader, which may limit rf gymnastics in MR, such as those introduced in Ref. [11], that aim to improve the emittance mismatch between RCS and MR.

During bunch rotation, the bunch ends rotate more slowly than the center due to the nonlinearity of the rf voltage, resulting in tail formation, a phenomenon well known in bunch compression techniques. However, in bunch lengthening methods using the V_{h4}, tail formation is mainly driven by the stretching process. Figure 8 shows the deformation process of the bunch shape during bunch lengthening. The contour lines in Fig. 8 are drawn according to the voltage pattern shown in Fig. 4. Panel (1) represents the initial phase-space distribution before lengthening. In order to visualize the deformation process of the particle distribution as a dependent variable on its initial position, phase space is transformed into polar coordinates ($r-\theta$), divided uniformly in θ, and particles

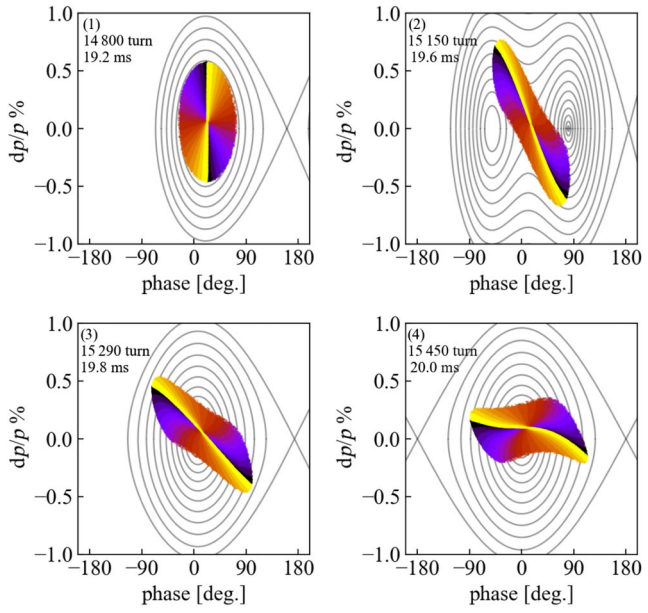


FIG. 8. Deformation process of the bunch shape during bunch lengthening. Panel (1) shows the initial distribution; particles in each sector are distinguished by different colors. Panel (2) shows the distribution during the application of the V_{h4}, panel (3) shows the distribution immediately after stopping the V_{h4}, and panel (4) shows the distribution after bunch rotation.

belonging to each angular sector are distinguished by different colors. Panel (2) shows the distribution during the application of the V_{h4} (just before it is stopped), panel (3) shows the distribution immediately after stopping the V_{h4}, and panel (4) shows the distribution after bunch rotation.

Yellow particles move along the contour lines associated with the UFP. Relative to the spreading direction of the yellow particles, particles on both sides (reddish and purplish) exhibit distinct behaviors. Reddish particles move toward the direction of the yellow particles. Purplish particles shift away from the direction of the yellow particles under the influence of the SFP contours on both sides of the UFP. In other words, Fig. 8 indicates a stretching process in which the tip of the bunch on the SFP side is attracted toward the SFP, while the opposite side remains unconfined and extends outward. This asymmetric stretching leads to the formation of tail precursors prior to bunch rotation. The asymmetry becomes more pronounced when the distance between the bunch and the SFPs is small. It is also enhanced when the voltage ratio V_{h4}/V_{h2} is high. However, as Fig. 7 shows, achieving a more stretched bunch (high B_f) requires a high voltage ratio. Further details of the bunch-shape deformation process are given in Appendix A.

B. Shape optimization strategy

To mitigate tail formation, a UFP pattern is investigated in which the V_{h4} is applied twice. The concept is illustrated in Fig. 9. The idea is that applying the V_{h4} twice modifies the formation process and thereby mitigates tail formation.

A method for creating a UFP pattern using a least-squares technique, a numerical optimization approach, is proposed. For the least-squares error function, six geometric parameters $(\Delta_1, \Delta_2, \cdots, \Delta_6)$ are defined, as shown in Fig. 10(a). From the four ϕ-coordinates of the intersections between the bunch contour and two lines parallel to the ϕ-axis—each passing through arbitrary points $(\pm \mathrm{d}p/p)$ on the $\mathrm{d}p/p$ axis—the following quantities are obtained: (i) Δ_1: Defined as the distance between the ϕ-coordinates of the intersections in the first and fourth quadrants. (ii) Δ_2: Defined as the distance between the ϕ-coordinates of the intersections in the second and third quadrants. (iii) Δ_3: Defined as the difference between Δ_1 and Δ_2.

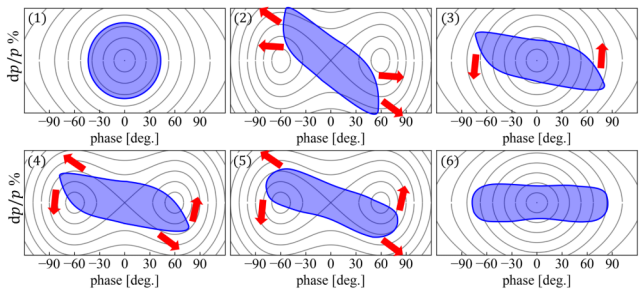


FIG. 9. Schematic of the bunch-shape deformation when the V_{h4} is applied twice. A two-stage process—stretching by the UFP generated via the V_{h4}, followed by rotation under the V_{h2}—is repeated. The tail formed during the first stage [from (1) to (3)] is smoothed in the second stage [from (4) to (6)].

From the four $\mathrm{d}p/p$-coordinates of the intersections between the bunch contour and two lines parallel to the $\mathrm{d}p/p$-axis—each passing through arbitrary points $(\pm\phi)$ on the ϕ axis—the following quantities are obtained: (i) Δ_4: Defined as the distance between the $\mathrm{d}p/p$-coordinates of the intersections in the first and second quadrants. (ii) Δ_5: Defined as the distance between the $\mathrm{d}p/p$-coordinates of the intersections in the third and fourth quadrants. (iii) Δ_6: Defined as the difference between Δ_4 and Δ_5.

When all six geometric parameters (Δ_1 through Δ_6) are zero, the bunch shape is circumscribed by two rectangles, as illustrated in Fig. 10(b).

The extraction bunch was calculated using BLonD and incorporated into the numerical optimization routine. The `least_squares` function from SciPy, a scientific computing library in Python, was employed [16]. Further supplementary explanation of the optimization procedure is given in Appendix B.

C. Shape optimization result

The parameters of the UFP pattern with the V_{h4} applied twice were optimized using the least-squares method. The start times and the application period of each V_{h4} were chosen as optimization variables. The voltage ratio (V_{h4}/V_{h2}) was fixed at 1.2, consistent with the UFP pattern shown in Table II, and the target B_f was set to 0.4. The optimized parameters are summarized in Table III, and the corresponding UFP pattern is illustrated in Fig. 11.

Compared with the UFP pattern in Fig. 4, the first V_{h4} application happens earlier, while the second is just before extraction. The bunch deformation process induced by two applications of the V_{h4} is shown in Fig. 12, with particles color-coded as in Fig. 8. Panels (1)–(3) correspond to the same deformation process as Fig. 8, while panel (4) corresponds to the timing of the V_{h4} reapplication after bunch rotation by the V_{h2}. Panel (5) shows the bunch shape after reapplication, and panel (6) shows the final shape, following the second rotation. As indicated by the deformation of the yellow particles, the tail formed up to

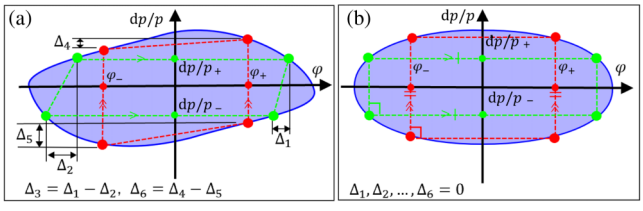


FIG. 10. Geometric parameters of the extracted bunch targeted for optimization. Panel (a) shows before and (b) after optimization.

TABLE III. Parameters of the UFP pattern with the V_{h4} applied twice, determined by the least-squares method.

Time (first)	19.32–19.50 ms
Time (second)	19.70–19.80 ms
Voltage ratio (first) (V_{h4}/V_{h2})	1.2
Voltage ratio (second) (V_{h4}/V_{h2})	1.2
Rise and fall time (first and second)	0.01 ms

panel (3) is bent toward the SFP side by the reapplied V_{h4}, and the tail formation is mitigated.

Figure 13 compares the outlines of the stretched bunches obtained with a single application and with two applications of the V_{h4}. The blue line represents the case with a single application of the V_{h4}, while the red line represents the case with two applications. By applying the V_{h4} twice, a bunch without sharp edges was formed. These results indicate that the tail, generated by asymmetric bunch deformation during bunch lengthening, can be mitigated by performing asymmetric stretching twice at different timings. In addition, they show that the UFP pattern can be determined by parameter optimization using the least-squares method.

When the extraction bunch contains a tail, filamentation occurs after MR injection, and oscillations in phase space are enhanced. To evaluate the difference in behavior of the phase-space distribution with and without the tail, the longitudinal beam profiles are compared for bunches with and without tails. In the following, a stretched bunch formed by a single application of the V_{h4} is referred to as a "bunch with tails," whereas a stretched bunch formed by two applications is referred to as a "bunch without tails." Figure 14 shows the phase-space distributions of these bunches after bunch rotation under the V_{h2}. Panels (a-1) and (b-1) present the bunch with tails and the bunch without tails, while panels (a-2) and (b-2) show the

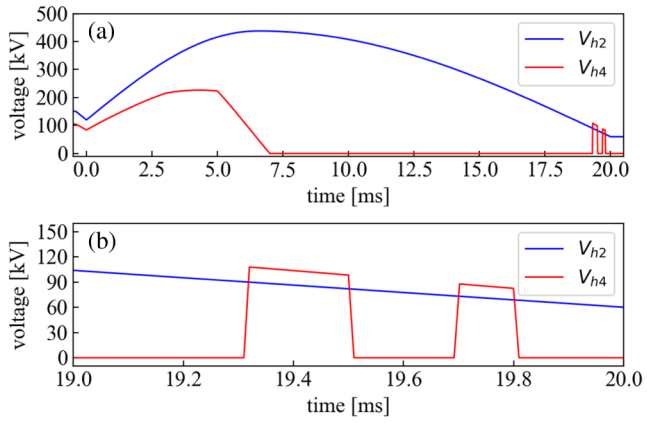


FIG. 11. The upper graph (a) shows the UFP pattern, in which the V_{h4} are applied twice. The lower graph shows an expanded view of the latter part of acceleration (19.0–20.0 ms) in the upper graph.

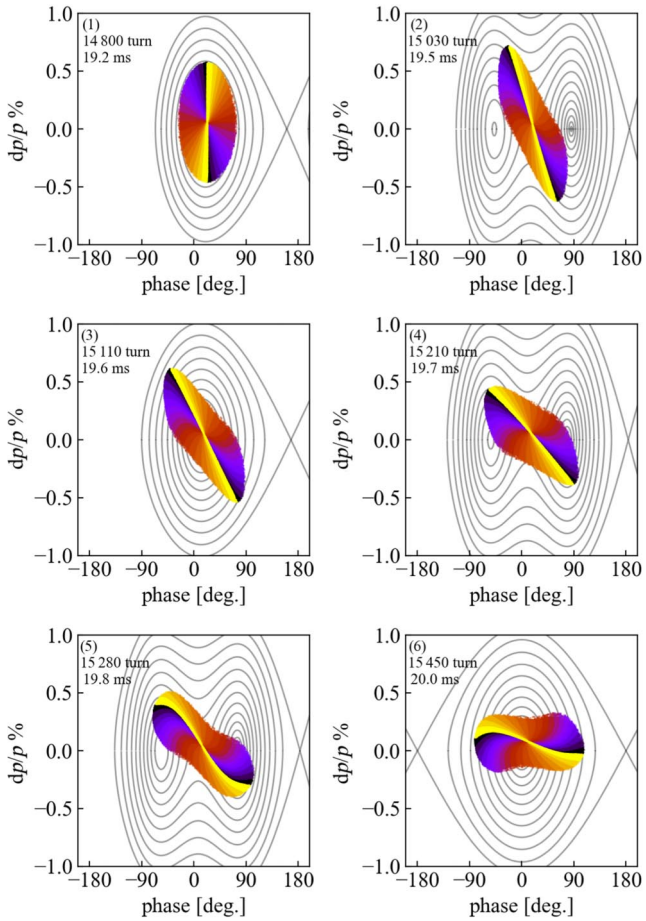


FIG. 12. Deformation process of the bunch shape during bunch lengthening with the V_{h4} applied twice. Panel (1) shows the initial distribution; particles in each sector are distinguished by different colors. Panel (2) shows the distribution during the application of the V_{h4}, panel (3) shows the distribution during bunch rotation, panel (4) shows the distribution just after reapplication of the V_{h4}, panel (5) shows the bunch deformed by the reapplied V_{h4}, and panel (6) shows the bunch shape after the subsequent bunch rotation.

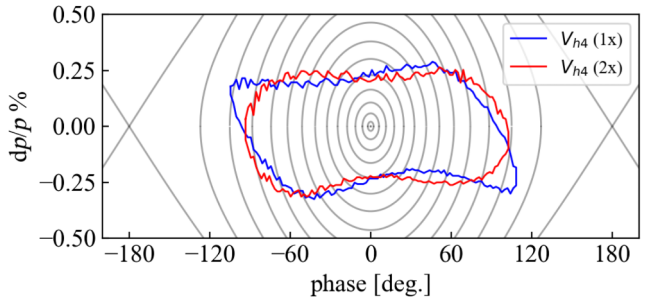


FIG. 13. Comparison of the stretched bunch shape depending on the number of applications of the V_{h4}. The blue line represents the case with a single application, while the red line represents the case with two applications. The bunch outline is obtained by connecting the outermost simulated particles.

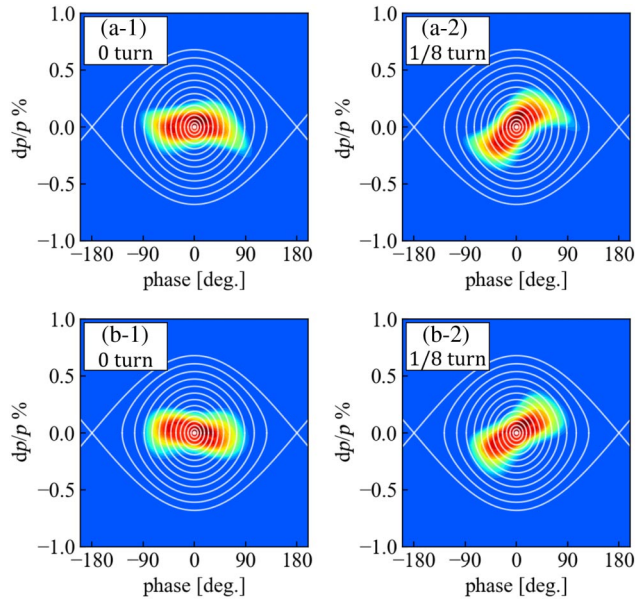


FIG. 14. Phase-space distributions of stretched bunches rotated with a 140-kV fundamental rf voltage. Panels (a-1) and (a-2) show the initial distribution of a stretched bunch with tails and its distribution after 1/8 bunch rotation. Panels (b-1) and (b-2) show the initial distribution of a stretched bunch without tails and its distribution after 1/8 bunch rotation.

distributions after an additional 1/8 bunch rotation. The bunch with tails exhibits more pronounced phase-space broadening than the bunch without tails. The extent of tail broadening can be evaluated through the smoothness of the rising and falling edges in the longitudinal beam profile. To quantify this smoothness, a fitting function based on the cumulative distribution function of a Gaussian was introduced.

$$F_{\mathrm{rise}} = \frac{1}{2}A_{\mathrm{rise}}\left[1 + \mathrm{erf}\left(\frac{t - t_{\mathrm{rise}}}{\sqrt{2}\,\sigma_{\mathrm{rise}}}\right)\right] + B_{\mathrm{rise}}, \tag{5}$$

$$F_{\mathrm{fall}} = \frac{1}{2}A_{\mathrm{fall}}\left[1 - \mathrm{erf}\left(\frac{t - t_{\mathrm{fall}}}{\sqrt{2}\,\sigma_{\mathrm{fall}}}\right)\right] + B_{\mathrm{fall}}, \tag{6}$$

$$\mathrm{erf}(x) = \frac{2}{\sqrt{\pi}}\int_0^x e^{-t^2}\,\mathrm{d}t. \tag{7}$$

Equation (5) gives the fitting function of the rising edge, and Eq. (6) gives the fitting function of the falling edge. Equation (7) indicates the error function. The parameters t_{rise} and t_{fall} denote the center times of the rising and falling transitions, respectively. The fitting parameters $A_{\mathrm{rise/fall}}$ represent the change in signal from the baseline to the final value, while $B_{\mathrm{rise/fall}}$ represent the baseline level. The values σ_{rise} and σ_{fall} represent the smoothness parameters of the rising and falling edges. They control the spread of the error function and thus determine how gradual the rising or falling edge is. Larger values correspond to smoother, more gradual transitions. The rising and falling edges of the beam profile during bunch rotation were fitted, and the values of σ_{rise} and σ_{fall} were obtained.

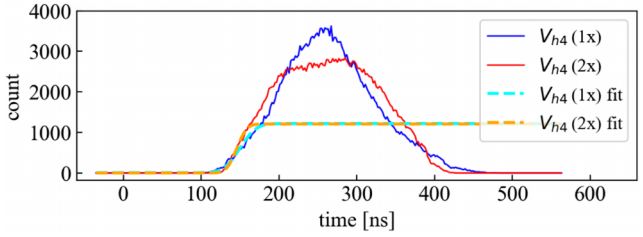


FIG. 15. Comparison of the calculated beam profiles after 1/8 bunch rotation. The blue and red lines represent the results for elongated bunches with and without tails, respectively. The cyan and orange dashed lines represent the corresponding fitting results obtained using Eq. (5).

Figure 15 shows the beam profile after 1/8 bunch rotation. The blue line represents the bunch with tails, whereas the red line represents the bunch without tails. The cyan line represents the fit to the rising edge of the blue line using Eq. (5), whereas the orange line represents the fit to the rising edge of the red line. As shown in Fig. 15, the bunch without tails exhibits a steeper rising edge. The falling edge was also fitted using Eq. (6). Figure 16 shows the values of σ_{rise} and σ_{fall} during 1/4 bunch rotation for the initial phase-space distributions with and without tails. As shown in Fig. 16, both σ_{rise} and σ_{fall} are larger for the bunch with tails than for the bunch without tails, indicating a smoother beam profile. Furthermore, σ_{fall} is larger than σ_{rise} for both cases. This asymmetry originates from the nonzero synchronous phase ϕ_s at the time when bunch lengthening is applied.

D. Advantages of bunch-shape optimization

To evaluate the advantages of suppressing the tail component in the extraction bunch, longitudinal beam simulations were performed after injection into MR. The MR rf bucket is formed by a dual-harmonic operation using the fundamental rf voltage V_{h9} and the second-harmonic rf voltage V_{h18}. Under the present

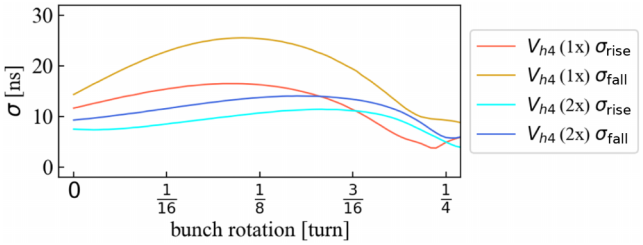


FIG. 16. Smoothness of the rising and falling edges of the calculated beam profile during 1/4 bunch rotation. The red and orange lines represent results for the bunch with tails in the initial phase-space distribution, while the blue and cyan lines represent results for the bunch without tails.

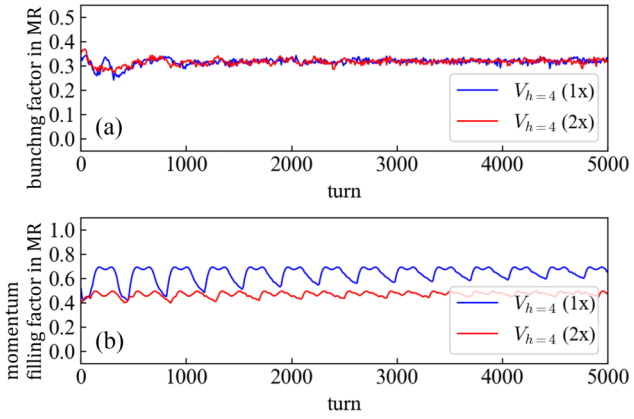


FIG. 17. Upper graph (a) shows B_f from injection into MR up to 5000 turns, while the lower graph (b) presents the MF factor. The blue line represents the result with tails, and the red line represents the result without tails.

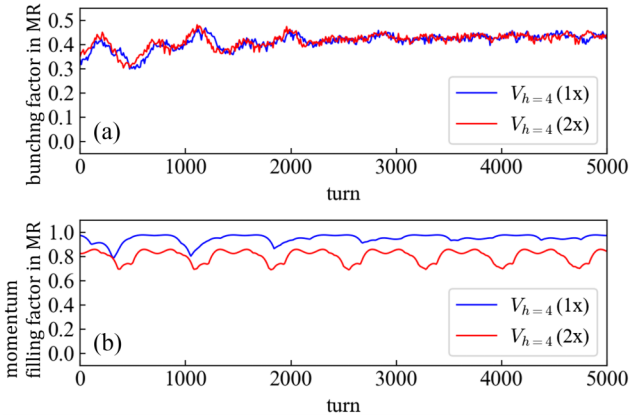


FIG. 18. The upper graph (a) shows B_f from injection into MR up to 5000 turns, while the lower graph (b) presents the MF factor. The blue line represents the result with tails, and the red line represents the result without tails.

MR operating conditions, the voltages are $V_{h9} = 140$ kV and $V_{h18} = 110$ kV, corresponding to a bucket area of approximately 15 eVs. Both the bunching factor B_f and the momentum filling factor (MF) were calculated. Where the MF is defined as:

$$\mathrm{MF} = \frac{(\text{the bunch height})}{(\text{the bucket height})}. \tag{8}$$

An MF value exceeding 1.0 indicates that a fraction of the particles spill out of the rf bucket. To realize acceleration without beam loss, the rf system is designed so that the maximum MF does not exceed approximately 0.8–0.9.

The results are shown in Fig. 17. The blue line represents the result using the bunch with tails, while the red line represents the result using the bunch without tails. No significant difference is observed in B_f. The MF results indicate that the tail drives oscillations, and its mitigation substantially reduces the MF oscillation amplitude. These calculations further support the results shown in Fig. 16, revealing that the tail responsible for the beam profile smoothness also drives large phase-space oscillations.

The benefit of tail mitigation in the rf gymnastics of MR was further examined. Figure 18 presents results obtained under the rf bucket condition $V_{h9} = 38$ kV and $V_{h18} = 30.8$ kV (corresponding to approximately 8 eVs). The blue line represents the bunch with tails, and the red line represents the bunch without tails. Although no significant difference is observed in B_f, the MR rf gymnastics drive B_f to converge to approximately 0.4. In the presence of a tail, MF approaches 1.0, indicating a high probability of beam loss. In contrast, tail mitigation reduces MF to approximately 0.85. These results indicate that tail mitigation achieved by applying the V_{h4} twice is effective for rf gymnastics in MR.

V. EXPERIMENTAL DEMONSTRATION

A. Bunch lengthening using second-harmonic rf voltage

A demonstration experiment of bunch lengthening was carried out in RCS. The beam experiment was performed using the operating parameters listed in Table IV and the UFP pattern listed in Table V.

Figure 19 shows the comparison of B_f between the experiment and the simulation. The simulations were carried out using BLonD. The simulations reproduce the experimental data well. It was demonstrated that the desired increase in B_f can be achieved by adjusting the voltage ratio and the application period of the V_{h4}.

TABLE IV. Simulation Conditions based on RCS operation parameters.

Intermediate pulse width	456 ns
Macropulse width	400 μs
Thinning	32/128
Intensity	8×10^{13} ppp
f_{rf} offset (injection and extraction)	0.0%/0.06%
LINAC momentum offset	−0.15%

TABLE V. Parameters of the UFP patterns adjusted to $B_f = 0.3$ and $B_f = 0.4$.

$B_f = 0.3$	Time	19.39–19.93 ms
	Ratio (V_{h4}/V_{h2})	0.5
	Rise and fall time	0.01 ms
$B_f = 0.4$	Time	19.32–19.76 ms
	Ratio (V_{h4}/V_{h2})	0.8
	Rise and fall time	0.01 ms

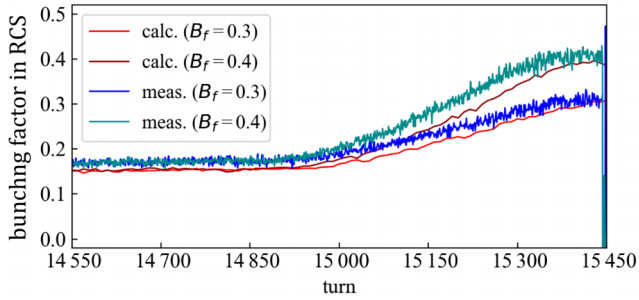


FIG. 19. Comparison of measured and simulated results for B_f. The blue line represents the measured values for a target $B_f = 0.3$, while the red line represents the corresponding simulation results. The cyan line represents the measured values for a target $B_f = 0.4$, and the brown line represents the corresponding simulation results.

The mountain plot of the experimental results is shown in Fig. 20. For comparison, longitudinal beam simulation results under the same conditions ($B_f = 0.4$) are also presented. Panels (a) and (b) show the experimental and simulation results, respectively. Figure 21 presents the beam profiles at the 15 000th turn (before bunch lengthening) and the 15 440th turn (just before extraction). The cyan line represents the experimental data, and the brown line represents the simulation results. The experimental results indicate that applying the V_{h4} stretched the bunch width at extraction, in good agreement with simulations. These findings demonstrate the bunch lengthening.

The measured voltage generated in the rf cavity is shown in Fig. 22. The timing and amplitude of the generated V_{h4} were confirmed to follow the programmed values. A slight distortion was observed during the rise and fall periods of the voltage waveform. This distortion shortens the effective stretching time of the UFP and reduces the B_f by a few percent. However, this reduction is negligibly small compared with the increase achieved by the bunch lengthening method.

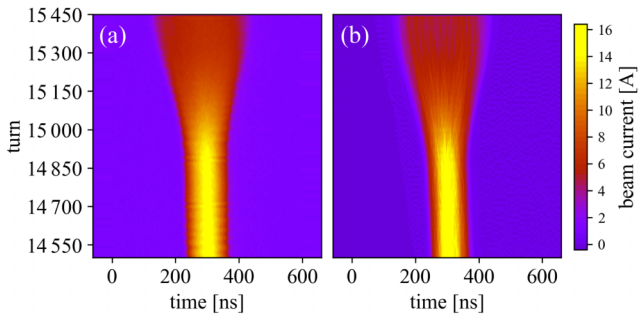


FIG. 20. Comparison between simulated and experimental mountain plot for a target $B_f = 0.4$. Panel (a) shows the experimental result, and panel (b) shows the calculated result. The plots are displayed from turns prior to the application of bunch lengthening.

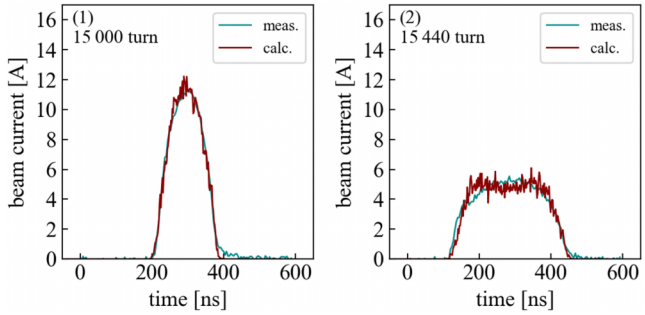


FIG. 21. Comparison between simulated and experimental beam profiles for a target $B_f = 0.4$. Panel (1) shows the profiles at 15 000 turns before the application of the V_{h4}, and panel (2) shows the profiles at 15 440 turns at the extraction position. The brown line represents the simulation results, while the cyan line represents the experimental data.

A demonstration was conducted in which beams with increased B_f produced by bunch lengthening were injected into MR. In this demonstration, a single-bunch extraction was employed instead of the standard two-bunch extraction mode from RCS to MR. The MR rf bucket was adjusted to match the RCS extraction bunches with $B_f = 0.3$ and $B_f = 0.4$. For the $B_f = 0.3$ case, the acceptance rf bucket was set to $V_{h9} = 110$ kV and $V_{h18} = 80$ kV (approximately 14 eVs), while for the $B_f = 0.4$ case, it was set to $V_{h9} = 38$ kV and $V_{h18} = 30.8$ kV (approximately 8 eVs).

The experimental results are shown in Fig. 23, together with the calculated results for comparison. Panel (a) corresponds to the injection of the RCS extraction bunch with $B_f = 0.3$, where the blue line represents the experimental data and the red line the calculation. Panel (b) corresponds to the $B_f = 0.4$ case, with cyan representing the experimental data and brown the calculation. For the $B_f = 0.3$ case, the beam exhibited only minor oscillations after injection and tended toward a value near 0.35.

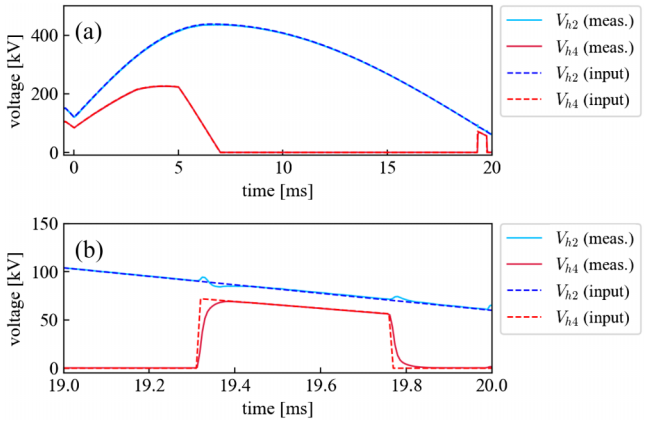


FIG. 22. Comparison of the measured voltage generated in the rf cavity with the acceleration pattern. The right graph shows the UFP pattern, an expanded view of the left graph.

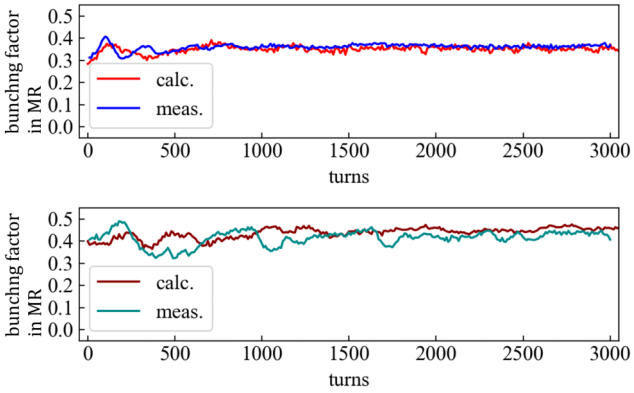


FIG. 23. Panel (a) shows the behavior of B_f up to 3000 turns after injection of the RCS extraction bunch with $B_f = 0.3$ into MR, while panel (b) shows the case for the $B_f = 0.4$. In each figure, the blue and cyan lines correspond to the experimental data, whereas the red and brown lines correspond to the calculated data.

For the $B_f = 0.4$ case, oscillations were larger than in the $B_f = 0.3$ case, but no local decrease was observed, and the B_f converged to approximately 0.4. The experimental results showed good agreement with the simulations. These findings demonstrate that bunch lengthening is effective in improving the matching between the RCS extraction bunches and the MR rf bucket.

B. Optimization of bunch shape

To verify the bunch-shape control method based on applying the V_{h4} twice-tomography [17], measurements were carried out in MR. The phase-space distribution, immediately after injection into the MR, was obtained. The MR rf bucket was composed of only the fundamental rf voltage V_{h9}, set to 140 kV. Figure 24 shows the measured phase-space distributions obtained in the tomography test. Panel (a) shows the distribution for injection without bunch lengthening. Panels (b) and (c) show the bunches corresponding to $B_f = 0.3$ and $B_f = 0.4$, when a single V_{h4} application was used. These bunches were formed using the UFP patterns generated from the parameters listed in Table V. Panels (d) and (e) show the results for the case of applying the V_{h4} twice, again with $B_f = 0.3$ and $B_f = 0.4$. The parameters of the UFP patterns used in these cases are listed in Table VI.

From panels (b) and (d), it is evident that the bunches stretched by bunch lengthening exhibit a phase-space distribution with a parallelogramlike shape, which means it has tails, consistent with the simulation results. In contrast, panels (c) and (e) demonstrate that bunches with the same B_f can be formed without a tail when the V_{h4} is applied twice. These observations show that the bunch-shape control method based on the double application of the V_{h4} enables the formation of the RCS-extracted bunches without tails. The bunch lengthening employing double application of the V_{h4} suggests an effective means of further improving the longitudinal beam matching between RCS and MR.

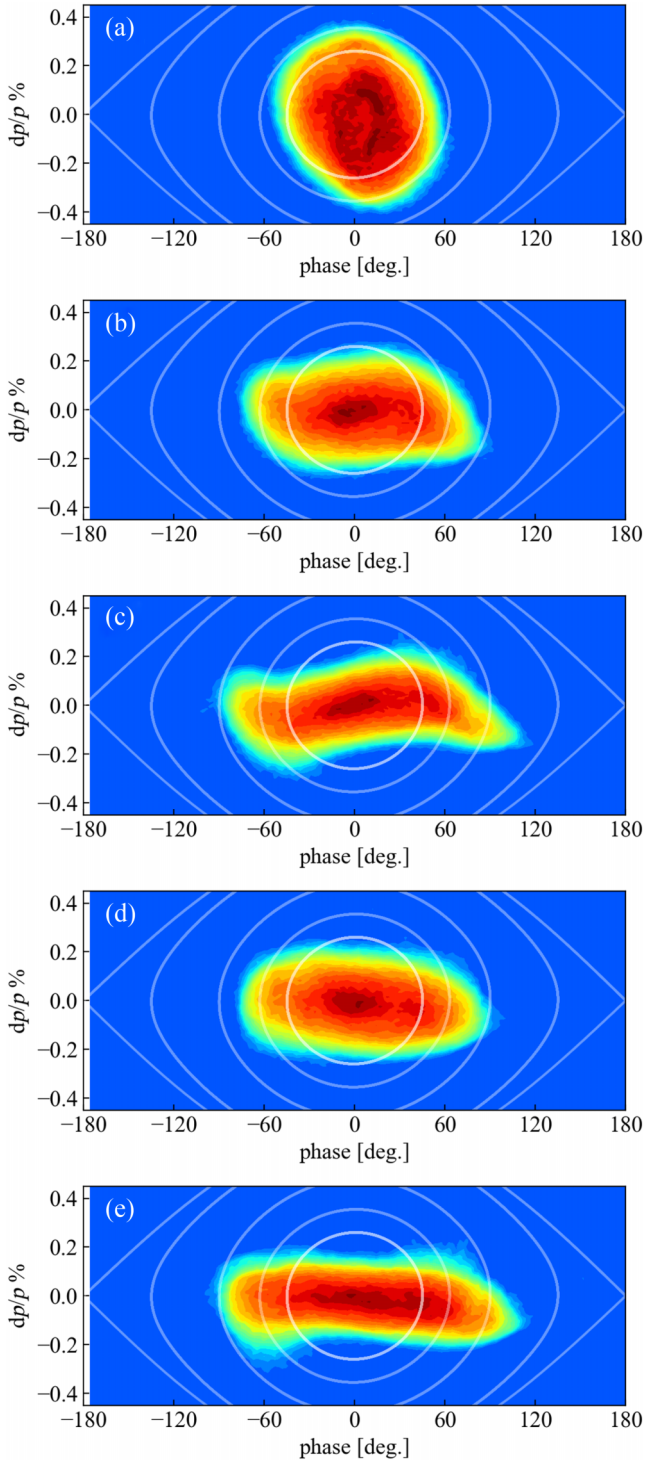


FIG. 24. Results of the tomography test. Panel (a) shows the distribution for injection without bunch lengthening. Panels (b) and (c) show bunches at $B_f = 0.3$ and $B_f = 0.4$ with a single V_{h4} application. Panels (d) and (e) show the corresponding results when the V_{h4} was applied twice.

TABLE VI. Parameters of the UFP patterns obtained with the application of the V_{h4} twice, adjusted to $B_f = 0.3$ and $B_f = 0.4$.

$B_f = 0.3$	Time (first)	19.38–19.65 ms
	Time (second)	19.85–19.95 ms
	Ratio (first) (V_{h4}/V_{h2})	0.8
	Ratio (second) (V_{h4}/V_{h2})	0.8
	Rise and fall time (first and second)	0.01 ms
$B_f = 0.4$	Time (first)	19.28–19.74 ms
	Time (second)	19.92–20.0 ms
	Ratio (first) (V_{h4}/V_{h2})	0.8
	Ratio (second) (V_{h4}/V_{h2})	0.8
	Rise and fall time (first and second)	0.01 ms

The phase-space distribution was reconstructed from beam profiles during bunch rotation with the fundamental rf voltage V_{h9} for MR. Consequently, the smoothness of the rising and falling edges of the beam profile can be evaluated in the same manner as in Sec. IV D. The tomography results for the $B_f = 0.4$ in Fig. 24, panels (c) and (e), were analyzed to evaluate the broadening of the beam profile. The smoothness parameter σ_{rise} and σ_{fall} for the rising and falling edges during $1/4$ bunch rotation were obtained from Eqs. (5) and (6). The results are presented in Figs. 25 and 26.

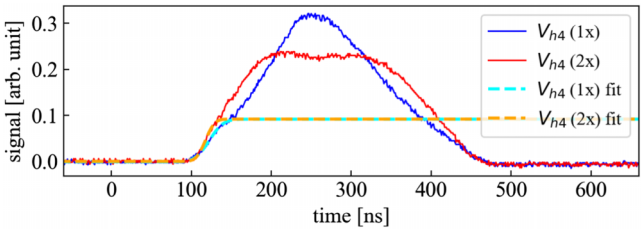


FIG. 25. Comparison of the measured beam profiles after $1/8$ bunch rotation. The blue and red lines represent the results for elongated bunches with and without tails, respectively. The cyan and orange dashed lines represent the corresponding fits obtained using Eq. (5).

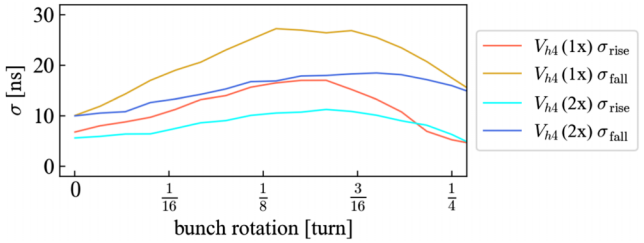


FIG. 26. Smoothness of the rising and falling edges of the measured beam profile after $1/4$ bunch rotation. The red and orange lines represent the result for the bunch with tails in the initial phase-space distribution, while the blue and cyan lines represent the result for the bunch without tails.

Figure 25 shows the beam profiles at $1/8$ bunch rotation together with the fitting results for the rising edge. The blue line represents the bunch with tails, while the red line represents the bunch without tails. The cyan and orange dashed lines represent the corresponding fits obtained using Eq. (5). Figure 26 presents the values of σ_{rise} and σ_{fall} for both the rising and falling edges during $1/4$ bunch rotation. Bunches with tails exhibit a smoother beam profile, whereas bunches without tails show a steeper profile. This result is consistent with the simulation results shown in Fig. 16. Moreover, the finding that σ_{fall} is larger than σ_{rise} also agrees with the simulation results. These observations strongly suggest that applying the V_{h4} twice during bunch lengthening mitigates tail formation. Using such bunches for MR injection suppresses large oscillations in the phase-space distributions.

VI. SUMMARY

The 3-GeV RCS at J-PARC supplies a high-intensity beam to the MR synchrotron. Under current operating conditions, the RCS extraction bunch is shorter than the MR rf bucket, and its B_f is quite low (approximately 0.2). This longitudinal mismatch has been the cause of beam loss. In order to improve the longitudinal beam matching between RCS and MR, a method was proposed to lengthen the bunch of the RCS extraction beam by utilizing the UFP generated by the second-harmonic rf voltage (V_{h4}) applied in the latter part of acceleration. Experiments on bunch lengthening with low-intensity beams in RCS demonstrated that the RCS extraction bunch can be stretched: the B_f increased from about 0.2 to roughly 0.4. Injection tests of the stretched bunches into MR showed that B_f within MR was maintained at approximately 0.3–0.4. Investigation of the stretching process revealed that the bunch-shape distortion (tails) can form during extension using the UFP with the V_{h4}. To mitigate tails, the application of the V_{h4} twice was considered. Both simulations and tomography measurements with low-intensity beams confirm that the bunch without tails, better adapted to the MR rf bucket, can be formed. These findings demonstrate an improvement in longitudinal beam matching between RCS and MR achieved by bunch lengthening. In the future, simulations and tests with high-intensity beams will be conducted to investigate the effects of higher-harmonic rf voltages on the increase of B_f and the modification of the lengthened bunch shape.

ACKNOWLEDGMENTS

LINAC, RCS, and MR provided stable beam conditions during the experimental demonstration of the bunch lengthening method. We are grateful to all members of the J-PARC LINAC, RCS, and MR teams for their support.

DATA AVAILABILITY

There are no publicly available research data or software supporting this manuscript. Requests for further information or data should be sent to the authors.

APPENDIX A: CONSIDERATIONS ON BUNCH STRETCHING PROCESS WITH UFP

Several cases of bunch stretching with nonadiabatic operations are presented in Fig. 27. Here, W is defined as $\Delta E/\omega_{rf}$ and can also be written as $W = (\mathrm{d}p/p) \times (\beta_s^2 E_s/\omega_{rf})$. All illustrations assume $\phi_s = 0$.

Figure 27(a) shows the rf bucket and the bunch when the V_{h4} with a voltage ratio that does not satisfy the condition in Eq. (4) is superimposed. The superposition widens the bottom of the potential, triggering bunch rotation, resulting in bunch stretching. Although an abrupt reduction of the fundamental rf voltage V_{h2} produces a similar deformation and lengthening, that scenario is not considered here.

Figure 27(b) shows the rf bucket and the bunch when V_{h4} is superimposed with a voltage ratio that satisfies Eq. (4). The superposition generates an UFP at the bunch center, resulting in bunch stretching.

Figure 27(c) shows the rf bucket and the bunch when no V_{h4} is applied, and the phase of the V_{h2} is jumped by π. The phase jump shifts the bunch onto the UFP, resulting in bunch stretching.

Figure 28 shows the bunch shape during stretching for each nonadiabatic operation. For simplicity, the initial bunch shape was assumed to be circular, with particles placed along its contour. In addition, $\phi_s = 0$ was adopted. Panel (a) corresponds to bunch stretching produced by widening the bottom of the potential through superposition

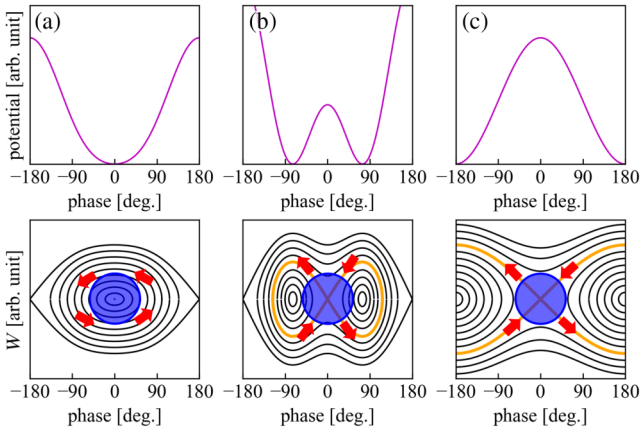


FIG. 27. The illustration shows three cases of nonadiabatic bunch stretching. Top row: potential; bottom row: bunch placed on contour lines before stretching; red arrows indicate motion. Panels (a) and (b) show the superposition of V_{h4} with voltage ratios that do not satisfy and that satisfy Eq. (4), respectively. Panel (c) shows the rf bucket and the bunch following a π phase jump of the V_{h2}.

of V_{h4}. Panels (b) and (c) correspond to UFP-based bunch stretching produced by superposition of V_{h4} (hereafter UFP_{h4} lengthening), while panel (d) shows UFP-based bunch stretching induced by a phase jump of V_{h2} (hereafter UFP_{h2} lengthening). The labels 1–5 indicate successive stages of time evolution. The time evolution of particles in the ϕ-W plane was computed using the following equation:

$$\frac{\mathrm{d}\phi}{\mathrm{d}t} = \frac{\omega_{\mathrm{rf}}^2 \eta}{\beta_s^2 E_s} W, \tag{A1}$$

$$\frac{\mathrm{d}W}{\mathrm{d}t} = \frac{eV_{h2}}{2\pi h}\left[\sin(\phi-\phi_{h2}) - \frac{1}{2}\frac{V_{h4}}{V_{h2}}\sin(2(\phi-\phi_s)) - \sin(\phi_s)\right], \tag{A2}$$

where parameter ϕ_{h2} represents the phase-offset of the V_{h2}. The corresponding parameters are listed in Table VII.

From these figures, the following observations can be made: (i) Compared with UFP_{h4} lengthening, UFP_{h2} lengthening produces an almost elliptical bunch shape with less distortion [e.g., panel (c-3) vs panel (d-3)]. (ii) In UFP_{h4} lengthening, a higher voltage ratio leads to faster and longer bunch extension [e.g., panel (a-5) vs panel (b-5)]. (iii) In UFP_{h4} lengthening, a higher voltage ratio results in a larger angle of the stretching direction [e.g., panel (b-5) vs panel (c-5)]. (iv) In UFP_{h4} lengthening, for a similar bunch length, UFP_{h4} lengthening with a lower voltage ratio yields less distortion [e.g., panel (b-5) vs panel (c-3)].

These characteristics can be explained as follows. Observation (1) arises because the distance between the UFP and the SFP is shorter in UFP_{h4} lengthening; consequently, UFP_{h2} lengthening also begins to distort when further evolved in time. Observations (2) and (3) are due to the dependence of the potential slope angle on the voltage ratio. Observation (4) results from the fact that a higher voltage ratio increases the angle between the vector directed toward the SFP and the stretching direction. A similar situation can also occur in UFP_{h2} lengthening, but its impact is less pronounced compared with UFP_{h4} lengthening.

In conclusion, to realize a less distorted bunch lengthening process in UFP_{h4} lengthening, it is necessary to choose as low a voltage ratio as possible. When a longer bunch length is required, however, a higher voltage ratio must be adopted, making the choice of parameters crucial for optimization.

To investigate the behavior of B_f and the bunch length in the panels (c) and (d) series of Fig. 28, the parabolic initial distribution shown in Fig. 29 was constructed. The red line represents the beam profile, which is evaluated using 100 bins. A total of 5×10^4 macroparticles were used, and the particles were color-coded according to their initial radial position to make their subsequent motion visually distinguishable. When the horizontal axis from

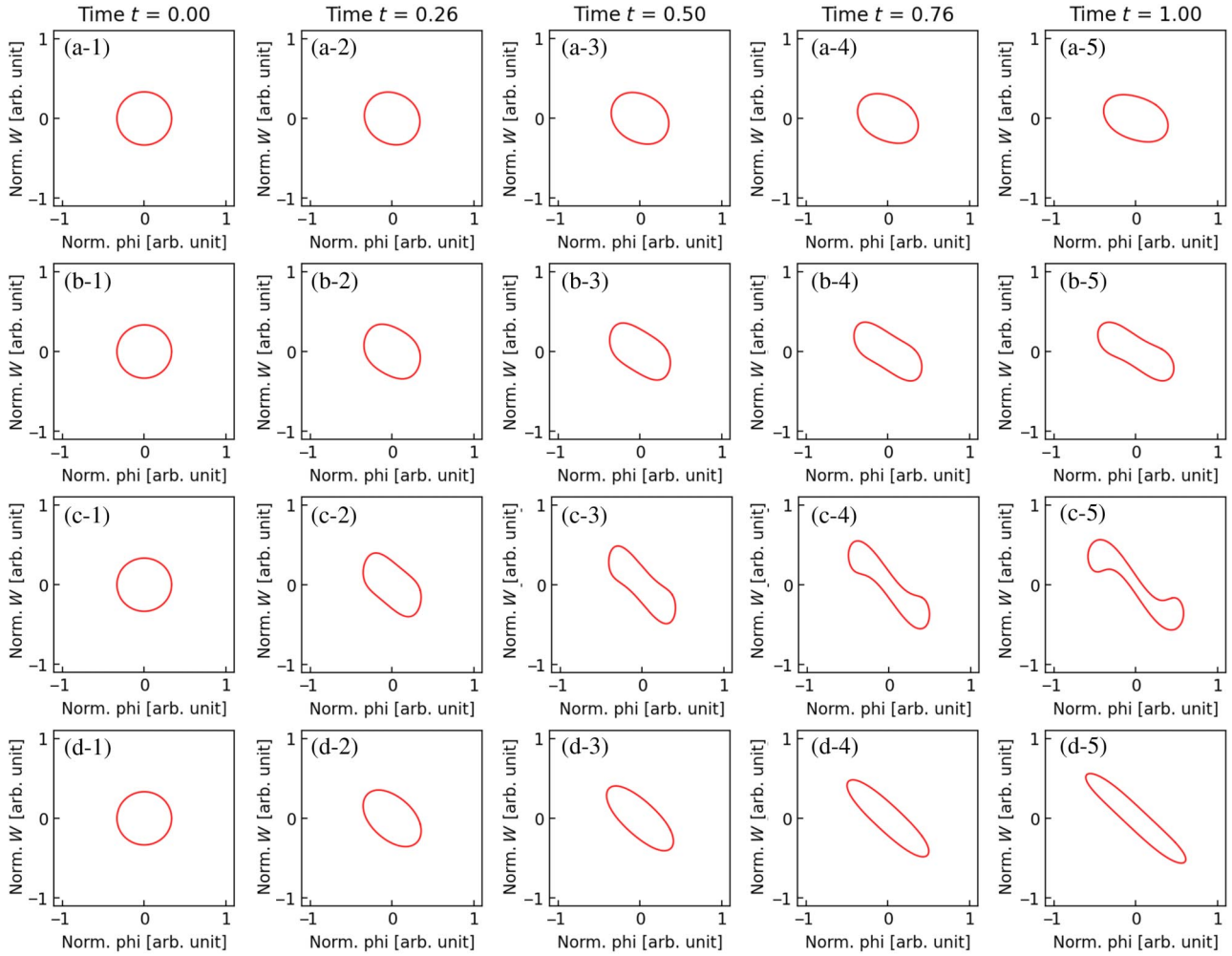


FIG. 28. Comparison of bunch lengthening processes driven by UFPs. Panels (a)–(c) show the evolution induced by UFPs generated by superimposing a second-harmonic rf voltage, with voltage ratios of 0.3, 0.8, and 1.8, respectively. Panel (d) shows the bunch lengthening process driven by a UFP created by applying a phase jump to the V_{h2}.

-1 to 1 is defined as one rf period, the B_f of the distribution in Fig. 29 is calculated to be $B_f = 0.25$.

Figure 30 presents the tracking results. For simplicity, $\phi_s = 0$ is assumed and the space-charge effects are neglected. Panels (a-1) and (a-2) show the bunch stretched by UFP$_{h4}$ lengthening, the phase-space distribution after the bunch rotation with V_{h2}, and each resulting beam profile. The voltage pattern is switched to bunch rotation at $t = 0.5$ from UFP$_{h4}$ lengthening. Panels (b-1) and (b-2) show the bunch stretched by UFP$_{h2}$ lengthening, the

TABLE VII. Parameter sets corresponding to Fig. 28.

Panel	UFP	V_{h4}/V_{h2}	ϕ_{h2}
(a-1)–(a-5)	UFP$_{h4}$	0.3	0
(b-1)–(b-5)	UFP$_{h4}$	0.8	0
(c-1)–(c-5)	UFP$_{h4}$	1.8	0
(d-1)–(d-5)	UFP$_{h2}$	0.0	π

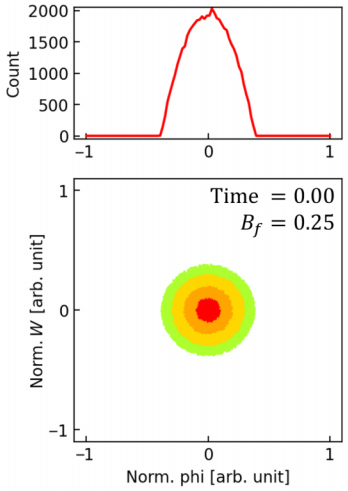


FIG. 29. Parabolic initial distribution consisting of 5×10^4 macroparticles. The particles are color-coded by their initial radius to visualize their subsequent motion. The beam profile is evaluated using 100 bins.

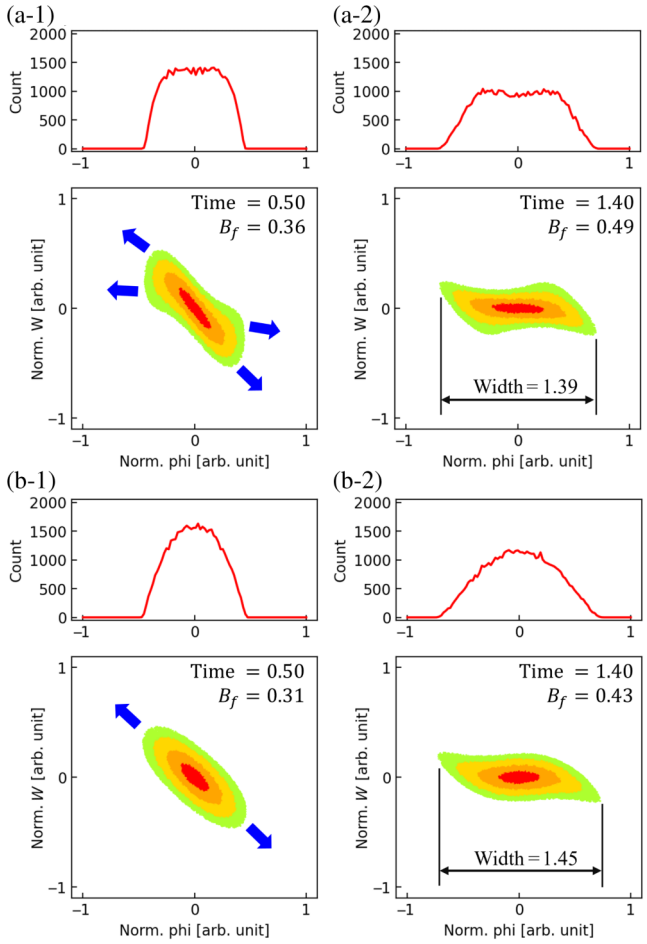


FIG. 30. Panels (a-1) and (a-2) show the bunch stretched by UFP_{h4} lengthening, followed by the phase-space distribution after the bunch rotation with V_{h2} and the resulting beam profile; the switching to bunch rotation occurs at $t = 0.5$. Panels (b-1) and (b-2) show the corresponding results for UFP_{h2} lengthening, with the switching time set to $t = 0.6$.

phase-space distribution after the bunch rotation with V_{h2}, and the resulting beam profile. The voltage pattern is switched to bunch rotation at $t = 0.6$ from UFP_{h2} lengthening.

As can be seen from the fact that particles farther from the radius form a more distorted distribution, particles closer to the SFP than those on the contour line passing through the UFP exhibit greater displacement toward the phase direction relative to the W direction. For UFP_{h2} lengthening, the positions of all particles are far from the SFP position, causing all particles to move nearly parallel to the particles on the contour line passing through the UFP. These differences result in UFP_{h4} lengthening transforming into a profile closer to a trapezoidal shape, whereas UFP_{h2} lengthening exhibits a profile change resembling a widened parabolic distribution. As a consequence, UFP_{h4} lengthening achieves a higher B_f than UFP_{h2} lengthening for the same stretched bunch length.

It is also noted that, even though UFP_{h2} lengthening does not form the tails during the stretching process, the tails appear after the bunch rotation due to the difference in rotation speed across the distribution (nonlinearity). This tail formation is attributed to the nonlinearity of the V_{h2}: a single-frequency sinusoidal.

APPENDIX B: OPTIMIZATION PROCEDURE

The optimization algorithm was the default trust-region reflective (TRF) method [18]. The TRF method provides a practical and stable approach for nonlinear least-squares problems involving bound constraints. The trust-region strategy stabilizes the step size even when the local quadratic model is poorly conditioned. Based on these properties, TRF was considered appropriate for the present bound-constrained optimization problem.

The optimization of the rf voltage pattern with bunch lengthening (hereafter referred to as the UFP pattern) was performed using the `least_squares` function of scipy.optimize. In this study, the TRF method was used as the optimization backend of `least_squares`. Given the residual vector $f(x)$ (an m-dimensional real function of n real variables) and a loss function $\rho(s)$, `least_squares` minimizes the cost function:

$$F(x) = \frac{1}{2}\sum_{i=0}^{m-1}\rho(f_i(x)^2), \tag{B1}$$

subject to the bound constraints $\mathrm{lb} \le x \le \mathrm{ub}$.

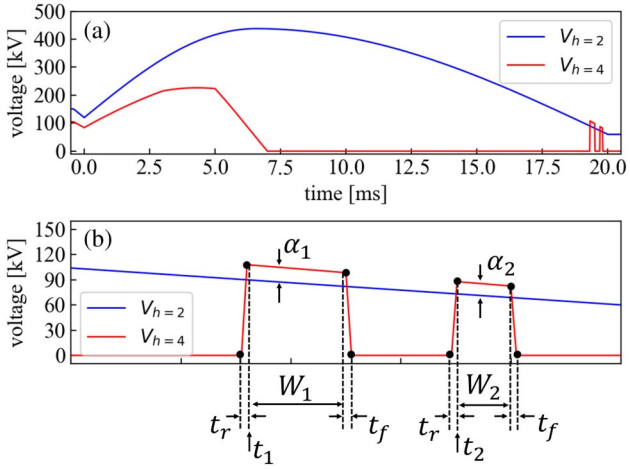


FIG. 31. Schematic definition of the UFP pattern parameters used in the optimization. The upper graph (a) shows the rf voltage pattern. The lower graph (b) shows an expanded view of the latter part of acceleration (19.0–20.0 ms) in the upper graph. The figure illustrates the timing and amplitude parameters of the second-harmonic rf voltage V_{h4}, including the start and end times of each application, the rise and fall times, and the voltage ratio ($\alpha = V_{h4}/V_{h2}$), which were used as design variables in the optimization procedure.

TABLE VIII. Definition of the UFP pattern parameters used in the optimization, corresponding to Fig. 31.

	First V_{h4}	Second V_{h4}
Start time	t_1	t_2
Driving time	W_1	W_2
Voltage ratio (V_{h4}/V_{h2})	α_1	α_2
Rise time	t_r	t_r
Fall time	t_f	t_f
Phase offset	$\Delta\phi_1$	$\Delta\phi_2$

In this study, the default linear loss function was used, corresponding to the standard nonlinear least-squares minimization of the sum of squared residuals. The residuals used in the optimization are the six geometric parameters $(\Delta_1, \Delta_2, \cdots, \Delta_6)$ defined in Sec. III. The cost function to be minimized is

$$F(x) = \sqrt{\Delta_1^2 + \Delta_2^2 + \Delta_3^2 + \Delta_4^2 + \Delta_5^2 + \Delta_6^2}. \tag{B2}$$

In practice, the implementation minimizes $\sum_{i=1}^{6} \Delta_i^2$, which is equivalent because the square root is a monotonic transformation.

The optimization variables (design parameters) are listed in Table VIII and illustrated in Fig. 31. These correspond to the UFP pattern in which the second-harmonic rf voltage V_{h4} is applied twice. The following quantities were treated as optimization variables: allowing all of these parameters to vary freely results in an excessively large search space and prevents stable convergence. Therefore, the following parameters were fixed based on physical considerations: (i) Rise and fall times: fixed at 0.01 ms. (ii) The phase of $\Delta\phi_{1,2}$: fixed at 0 for simplicity.

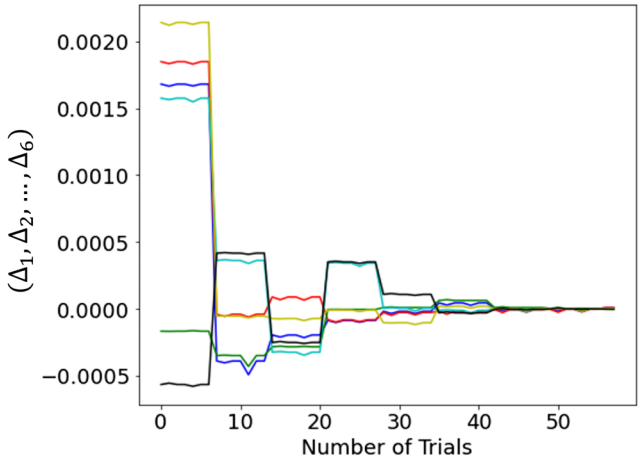


FIG. 32. Convergence of the geometric parameters $(\Delta_1, \Delta_2, \cdots, \Delta_6)$ with iteration number in the optimization process.

In some cases, certain parameters were treated as fixed values rather than optimization variables, when doing so provided practical simplification of the search space and improved convergence stability. Bound constraints were imposed on the free parameters: the voltage ratio was restricted to $0 \le V_{h4}/V_{h2} \le 2$, and the start times were limited to $15 \le t_{1,2} \le 20$ ms.

A representative convergence example is shown in Fig. 32. As the iterations proceed, each geometric parameter Δ_i approaches zero, indicating that the bunch shape becomes closer to the desired rectangular profile.

Because the optimization problem is highly nonlinear, the convergence exhibits strong dependence on the initial parameter values. For this reason, a broad parameter scan is effective for identifying suitable initial guesses, while the nonlinear least-squares method is well suited for subsequent local refinement.

[1] H. Hotchi *et al.*, Beam commissioning of the 3-GeV rapid cycling synchrotron of the Japan Proton Accelerator Research Complex, Phys. Rev. ST Accel. Beams **12**, 040402 (2009).
[2] K. Yamamoto *et al.*, Design and actual performance of J-PARC 3-GeV rapid cycling synchrotron for high-intensity operation, J. Nucl. Sci. Technol. **59**, 1174 (2022).
[3] T. Koseki *et al.*, Beam commissioning and operation of the J-PARC main ring synchrotron, Prog. Theor. Exp. Phys. **2012**, 02B004 (2012).
[4] S. Igarashi *et al.*, Accelerator design for 1.3-MW beam power operation of the J-PARC Main Ring, Prog. Theor. Exp. Phys. **2021**, 033G01 (2021).
[5] H. Klingbeil, U. Laier, and D. Lens, *Theoretical Foundations of Synchrotron and Storage Ring RF Systems* (Springer, New York, 2015).
[6] T. Yasui *et al.*, Transverse emittance growth caused by space-charge-induced resonance, Phys. Rev. Accel. Beams **23**, 061001 (2020).
[7] H. Hotchi, Beyond 1-MW beam operation of J-PARC Main Ring, J. Phys. Soc. Jpn. Conf. Proc. **45**, 011115 (2026).
[8] J. Griffin *et al.*, Time and momentum exchange for production and collection of intense antiproton beams at Fermilab, IEEE Trans. Nucl. Sci. **30**, 2630 (1983).
[9] R. Garoby, A non-adiabatic procedure in the PS to supply the nominal proton bunches for LHC into 200 MHz RF buckets in SPS, Tech. Rep., PS/RF/Note 93-17, CERN, 1993.
[10] R. Garoby, Rf gymnastics in synchrotrons, CERN Yellow Report CERN-2011-007, CERN, Geneva, Switzerland, 2011, pp. 431–446.
[11] H. Okita *et al.*, Consideration for improving the longitudinal beam matching between RCS and MR at the J-PARC, J. Phys.: Conf. Ser. **3094**, 012027 (2025).

[12] C. Ohmori *et al.*, Development of a high gradient rf system using a nanocrystalline soft magnetic alloy, Phys. Rev. ST Accel. Beams **16**, 112002 (2013).

[13] F. Tamura *et al.*, Commissioning of the next-generation LLRF control system for the Rapid Cycling Synchrotron of the Japan Proton Accelerator Research Complex, Nucl. Instrum. Methods Phys. Res. A **999**, 165211 (2021).

[14] F. Tamura *et al.*, Multiharmonic vector rf voltage control for wideband cavities driven by vacuum tube amplifiers in a rapid cycling synchrotron, Phys. Rev. Accel. Beams **22**, 092001 (2019).

[15] H. Timko *et al.*, Beam longitudinal dynamics simulation studies, Phys. Rev. ST Accel. Beams **26**, 114602 (2023).

[16] https://docs.scipy.org/doc/scipy/reference/generated/scipy.optimize.least_squares.html.

[17] H. Okita *et al.*, Improvement of the longitudinal phase space tomography at the J-PARC synchrotrons, J. Phys.: Conf. Ser. **2687**, 072005 (2024).

[18] T. F. Coleman and Y. Li, An interior trust region approach for nonlinear minimization subject to bounds, Tech. Rep., TR 93-1342, Cornell University, 1993.